

Visualizing transient low-populated structures of RNA

Elizabeth A. Dethoff^{1*}, Katja Petzold^{1*}, Jeetender Chugh^{1*}, Anette Casiano-Negroni^{1†} & Hashim M. Al-Hashimi¹

The visualization of RNA conformational changes has provided fundamental insights into how regulatory RNAs carry out their biological functions. The RNA structural transitions that have been characterized so far involve long-lived species that can be captured by structure characterization techniques. Here we report the nuclear magnetic resonance visualization of RNA transitions towards ‘invisible’ excited states (ESs), which exist in too little abundance (2–13%) and for too short a duration (45–250 μ s) to allow structural characterization by conventional techniques. Transitions towards ESs result in localized rearrangements in base-pairing that alter building block elements of RNA architecture, including helix–junction–helix motifs and apical loops. The ES can inhibit function by sequestering residues involved in recognition and signalling or promote ATP-independent strand exchange. Thus, RNAs do not adopt a single conformation, but rather exist in rapid equilibrium with alternative ESs, which can be stabilized by cellular cues to affect functional outcomes.

Nuclear magnetic resonance (NMR) relaxation dispersion methods^{1,2}, which measure microsecond-to-millisecond conformational exchange, have made it possible to characterize the transient, low-populated excited state (ES) structures of proteins^{2,3} and to establish their importance in catalysis⁴, folding^{5,6}, signalling⁷ and recognition⁸. These ESs exist in too little abundance (typically with populations <5%) and for too short a duration (lifetime < milliseconds) to allow structural characterization by conventional techniques. Recent advances that extend the timescale sensitivity of rotating frame ($R_{1\rho}$) carbon relaxation dispersion experiments have made it possible to characterize fully exchange processes in nucleic acids^{9–11}, culminating in the discovery of ES Hoogsteen base pairs in DNA¹². Although evidence for RNA ESs has been reported for decades, their structure and role in function have remained elusive^{13–15}.

Here we report a strategy for characterizing the ES structures of RNA that combines $R_{1\rho}$ NMR experiments, mutagenesis and secondary structure prediction. With this approach, we visualized ES structures for three distinct RNAs and obtained insights into their biological functions.

ES structure of the HIV TAR apical loop

We used a low spin-lock field $R_{1\rho}$ NMR experiment^{9–11} to measure microsecond-to-millisecond conformational exchange at sugar (C1') and nucleobase (C8 and C6) carbon sites in the well studied hexanucleotide apical loop of the transactivation response element (TAR)¹⁶ from the human immunodeficiency virus type-1 (HIV-1). The TAR apical loop is a flexible recognition site that allows adaptive binding to a variety of proteins¹⁷. We observed conformational exchange (Fig. 1b and Supplementary Fig. 1) at carbon sites spread throughout the entire TAR apical loop (Fig. 1a). The $R_{1\rho}$ data could be collectively fitted to a two-state ($\text{GS} \xrightleftharpoons[k_{-1}]{k_1} \text{ES}$) exchange process (where GS indicates ground state) that is directed towards an ES with population $p_{\text{ES}} \approx 13\%$ and lifetime ($\tau_{\text{ES}} = 1/(k_{-1}) \approx 45 \mu\text{s}$) (Supplementary Table 1). A slower exchange process is observed at C1' of G33 (G33–C1'), G33–C8 and A35–C8 ($p_{\text{ES}} < 1\%$ and $\tau_{\text{ES}} = 1.9\text{--}2.3 \text{ ms}$), which can be assigned to a distinct higher energy ES that will not be discussed further (Supplementary Discussion and Supplementary Fig. 5).

In the ground state (GS), apical loop residues exist in equilibrium between C2'-endo and C3'-endo sugar pucker, G34 forms a flexible cross-loop C30•G34 Watson–Crick (WC) base pair, whereas the bases of U31, G32 and A35 are flexible^{18,19}. To gain insights into the ES structure, we examined the sugar and base ES carbon chemical shifts (ω_{ES}) obtained from the two-state analysis of the $R_{1\rho}$ data, which are sensitive reporters of base stacking, sugar pucker and *syn* versus *anti* glycosidic angles²⁰. The downfield-shifted sugar ES C30–C1', U31–C1' and A35–C1' chemical shifts strongly suggest that in the ES these residues adopt a pure C3'-endo sugar pucker characteristic of a helical conformation (Fig. 1a and Supplementary Table 1). The downfield-shifted base ES G34–C8 can unambiguously be assigned to a *syn* base²¹ (Supplementary Discussion) and has a chemical shift that is highly characteristic of a UUCG tetraloop, which features a *trans*-wobble G•U base pair (underlined) and a *syn* base (italics)²². Notably, TAR can accommodate a similar U₃₁G₃₂G₃₃G₃₄ tetraloop. This places G34 in a *syn* position, where it can base pair with U31, thus explaining exchange at U31–C6. It also leads to the formation of C30•A35 and U31•G34 non-canonical closing base pairs, explaining the helical conformation observed for these residues in the ES. Transitions towards this ES require disruption of the cross-strand C30•G34 base pair, explaining the measured activation free energy (12.6 kcal mol^{−1}) (Supplementary Fig. 2), which is at the low end of the free energy range required to open RNA WC base pairs (13–16 kcal mol^{−1})²³. This ES is also predicted to be the second most energetically favourable conformation using the secondary structure prediction program MC-Fold²⁴ (Supplementary Fig. 3).

We used a ‘mutate-and-chemical-shift-fingerprint’ (MCSF) strategy to test the proposed TAR ES. Here, a mutation or chemical modification is introduced to stabilize (or destabilize) a candidate ES, and the mutant's NMR carbon chemical shift fingerprints are compared with those of the ES (or GS). We stabilized the proposed TAR ES using two point mutations, C30U (TAR(C30U)) and A35G (TAR(A35G)), that replace the ES C30•A35 non-canonical base pair with more stable WC U30•A35 and C30•G35 base pairs, respectively (Fig. 1c). Both mutants adopted the proposed ES structure, as confirmed by NMR

¹Department of Chemistry & Biophysics, University of Michigan, 930 North University Avenue, Ann Arbor, Michigan 48109-1055, USA. [†]Present address: NYMIRUM, 3510 West Liberty Road, Ann Arbor, Michigan 48103, USA.

*These authors contributed equally to this work.

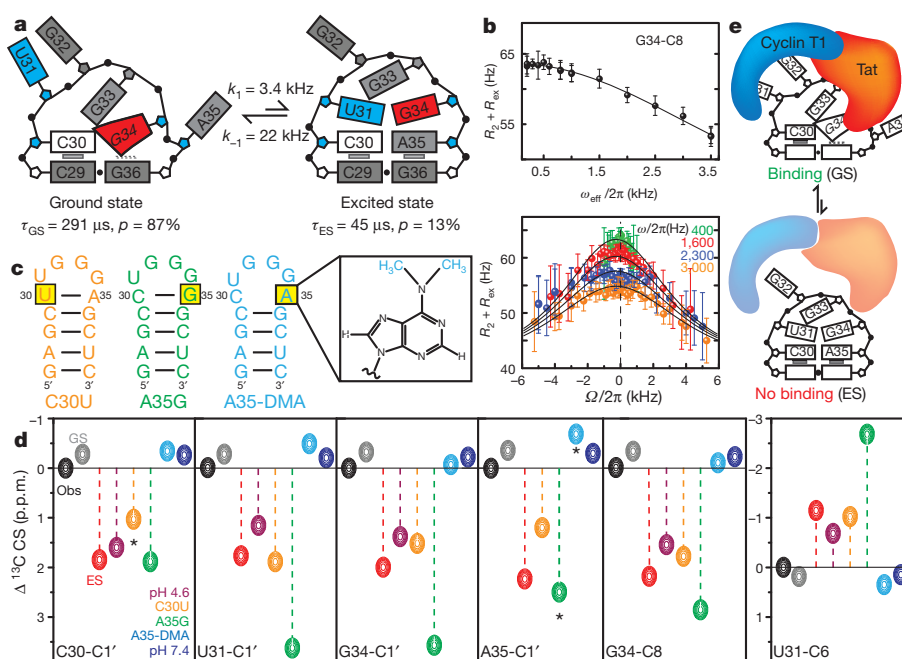


Figure 1 | Excited-state structure of the HIV-1 TAR apical loop. **a**, GS and ES structures of TAR. ES chemical shifts indicating increased stacking and/or *anti* glycosidic angles and C3'-endo sugar pucker are blue; decreased stacking and/or *syn* glycosidic angles and non-C3'-endo sugar pucker are red. Sites with little to no fast exchange are grey. **b**, Example relaxation dispersion profile showing dependence of $R_2 + R_{ex}$ on spin-lock power ($\omega_{eff}/2\pi$) and offset

($\Omega/2\pi$), where Ω is the difference between the observed resonance frequency and the spin-lock carrier frequency. Shown is a global fit (solid line) to a two-state Laguerre equation. Error bars indicate one s.d. **c**, Mutant mimics of GS and ES. **d**, Comparison of carbon chemical shifts (CS) for the ES, GS and mutant mimics. Carbons at the site of mutation are indicated using an asterisk. **e**, Proposed functional role for TAR ES.

(Supplementary Fig. 4), and relative to wild-type TAR both mutants featured large changes in the carbon chemical shifts, specifically at sites showing fast exchange in wild-type TAR, that are directed towards the ES chemical shifts (Fig. 1d). Inversely, we destabilized the ES by introducing a bulky N6-N6-dimethyl-substituent at the A35-N6 position (TAR(A35-DMA)) (Fig. 1c), which impairs formation of the ES C30•A35 base pair without affecting the bulged-out A35 GS conformation. This modification quenched the chemical exchange (Supplementary Fig. 1) and resulted in oppositely shifted chemical shift perturbations that are directed towards the GS (Fig. 1d). It also allowed observation of the A35-C2H2 resonance, which was otherwise severely exchange-broadened (Supplementary Fig. 4), possibly due to protonation of A35-N1 and formation of a protonated ES A35⁺•C30 wobble base pair^{15,25}. Indeed, we were able to stabilize the ES by reducing the pH from 6.4 to 4.6, as verified by analysis of carbon chemical shifts and nuclear Overhauser effects (Fig. 1d and Supplementary Figs 1 and 4). Conversely, increasing the pH to 7.4 stabilized the GS and quenched the chemical exchange (Fig. 1d and Supplementary Fig. 1).

What is the functional significance of the TAR ES? The ES sequesters U31, G34, C30 and A35 into base pairs, such that they are no longer available to bind the viral transactivator protein Tat and human cyclin T1 (Fig. 1e), which together activate transcription of the HIV-1 genome. Notably, analysis of previous mutations reveals that mutants that stabilize the TAR ES inhibit Tat/cyclin T1 binding and transcriptional activation, whereas mutants that do not stabilize the ES have little to no effect^{26–28} (Supplementary Fig. 6). The TAR ES is destabilized relative to the GS by only ~ 1.1 kcal mol^{−1} (Supplementary Fig. 2), and can readily become $>50\%$ populated upon binding to one of several proteins known to bind TAR and interact with the apical loop¹⁷, or by other physiochemical parameters such as the lowering of pH. The TAR ES may be involved in downregulating transactivation of the HIV genome or provide a mechanism for releasing Tat and cyclin T1. Although these functional roles remain to be verified, stabilizing the autoinhibited TAR ES immediately provides a new route for targeting TAR in the development of anti-HIV therapeutics.

ES structure of the ribosomal A-site

We used our strategy to characterize the ES structure of the ribosomal A-site internal loop²⁹ (Fig. 2a). The A-site has essential roles in decoding messenger RNA by flipping out two internal-loop adenines (A1492 and A1493, referred to hereafter as A92 and A93), which interact with and stabilize the codon–anticodon mini-helix formed between the cognate aminoacyl tRNA and mRNA^{29,30} (see Fig. 2e). We observed extensive carbon chemical exchange at seven residues within and below the A-site internal loop (Fig. 2a, b and Supplementary Fig. 1). A two-state analysis of the $R_{1\rho}$ data revealed a global exchange process directed towards an ES with population $p_{ES} \approx 2.5\%$ and lifetime $\tau_{ES} = 1/k_{-1} \approx 248$ μ s (Supplementary Table 1).

Biophysical studies show that in the GS, A92 is looped inside, probably forming a base pair with A08, whereas A93 is partially flipped out and flexible³¹ (Fig. 2a). An ES involving the flipping out of A92 and A93, as observed in several X-ray and NMR structures of drug-bound A-site³², can be ruled out based on the observation of exchange below the internal loop, ES chemical shift fingerprints that suggest increased stacking for A93 (Supplementary Fig. 5), and by comparison of ES chemical shifts with those of drug-bound A-site (Supplementary Fig. 7).

Rather, the breadth of exchange across many different residues points to a larger structural rearrangement. The downfield-shifted base ES chemical shift for U95-C6 indicates looping out of U95, whereas the upfield-shifted base carbon ES chemical shifts indicate increased stacking for A92, A93, G94 and C96 (Fig. 2a and Supplementary Table 1). These data can be explained by an alternative structure in which U95 bulges out while A93•C07, G94•U06 and A08•A92 form three consecutive non-canonical base pairs (Fig. 2d and Supplementary Table 1). A transition towards such an ES requires the opening of C07•G94, explaining the sizable free-energy barrier of ~ 14.8 kcal mol^{−1} (Supplementary Fig. 2)²³. This ES is predicted by MC-Fold to be the second most energetically favourable secondary structure (Supplementary Fig. 3) and has previously been observed in molecular dynamics simulations³³.

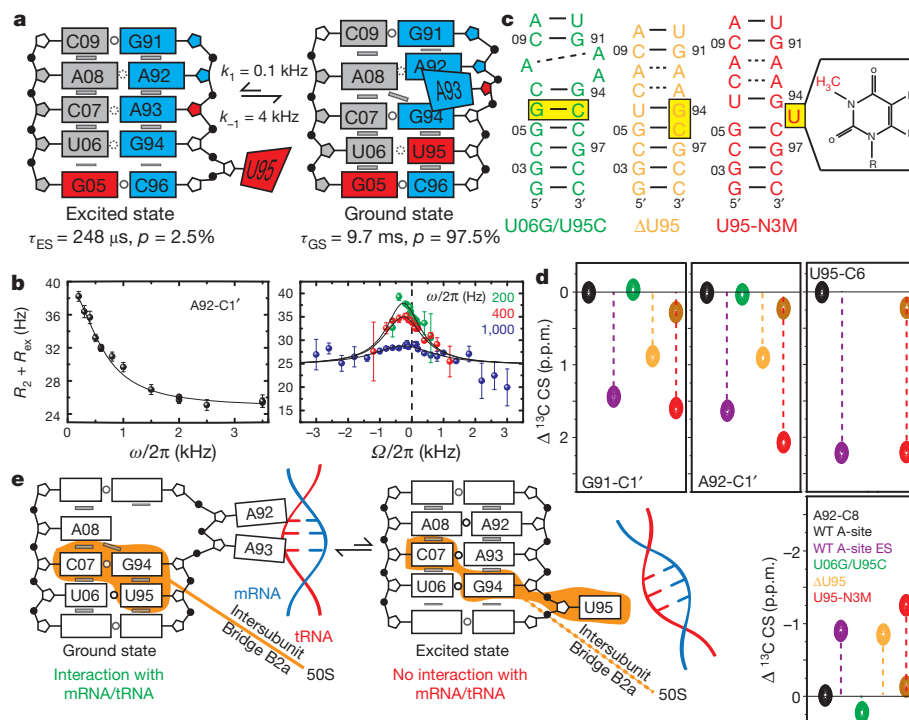


Figure 2 | Excited-state structure of the ribosomal A-site internal loop. **a**, GS and ES structures of the A-site. Chemical shift fingerprints are colour-coded as in Fig. 1a. **b**, Example relaxation dispersion profile (as in Fig. 1b).

We confirmed the proposed A-site ES using MCSF analysis. We were able to block transitions towards the ES by replacing U06•U95 with a more stable WC G06•C95 base pair (A-site(U06G/U95C)) (Fig. 2c). This locked the A-site into the GS as judged by the GS-like chemical shifts (Fig. 2d and Supplementary Fig. 5) and absence of chemical exchange, including at sites (for example, A92 and A93) that are distant from the site of mutation (Supplementary Fig. 1). This also confirmed that all sites experience a common global exchange process. We then stabilized the proposed ES by deleting U95, which bulges out in the ES (A-site(ΔU95)), and by introducing a methyl group at U95-N3 (A-site(U95-N3M)), which is expected to disrupt the GS U06•U95 non-canonical base pair in favour of the bulged-out ES conformation (Fig. 2c). The A-site(ΔU95) mutant adopted the proposed ES structure as confirmed by NMR (Supplementary Fig. 4) and resulted in large changes in the carbon chemical shifts specifically at sites showing exchange that are directed towards the ES chemical shifts (Fig. 2d and Supplementary Fig. 5). More dramatically, the A-site(U95-N3M) mutant exhibited two equally populated sets of resonances in slow exchange on the NMR timescale (Supplementary Fig. 4), with one set corresponding to the GS and the other in near-perfect agreement with the ES (Fig. 2d and Supplementary Fig. 5).

The A-site ES sequesters A92 and A93 into base pairs, making them unavailable to decode mRNA. It also affects the structural presentation of A-site residues involved in protein recognition and formation of the B2a intersubunit crossbridge (Fig. 2a, e). Thus, we analysed previous mutational data in light of the ES A-site structure determined here. Interestingly, mutants that are predicted to stabilize the A-site ES increase the rates of stop-codon readthrough and frame-shifting, both of which are processes that can bypass mRNA decoding³⁴ or inhibit binding of initiation factor 1³⁵ (Supplementary Fig. 6). In addition, the introduction of chemical groups at the U95-N3 position, a modification that is analogous to that which we used to trap the A-site ES, leads to severely impaired association of ribosomal subunits *in vitro* due to disruption of the B2a intersubunit crossbridge³⁶. This provides strong evidence that the A-site ES can form within the ribosome context

c, Mutant mimics of GS and ES. **d**, Comparison of carbon chemical shifts for the ES, GS and mutant mimics. **e**, Proposed functional role for A-site ES.

where it can affect function. Although X-ray structures of the ribosome show the A-site in a GS-like conformation, in several cases, the electron density at the A-site is poor as judged by elevated B-factors, and can accommodate the ES conformation determined here (data not shown). The A-site ES invites reassessment of the A-site region in current ribosome structures and suggests a new route for targeting the A-site in the development of antibiotics.

Two ES structures in HIV-1 stem loop 1

Finally, we used our strategy to study the ES structure of the HIV-1 stem loop 1 (SL1) (Fig. 3a). SL1 spontaneously forms kissing dimers, which isomerize during viral maturation into more stable duplex dimers through mechanisms that remain poorly understood^{37–39} (see Fig. 3e). This isomerization requires the melting and re-annealing of the SL1 hairpin and is catalysed *in vivo* by the nucleic acid chaperone nucleocapsid protein, but can also occur spontaneously *in vitro*^{39–41}. A highly conserved asymmetric SL1 internal loop is essential for both nucleocapsid-dependent and spontaneous isomerization⁴², and has been shown to induce complex NMR chemical exchange^{43,44}.

We observed extensive conformational exchange in a monomeric SL1 construct (SL1m)^{43,45} spanning 7 base pairs in and around the internal loop (Fig. 3a, b and Supplementary Fig. 1). Unlike the A-site, the exchange extends to residues both below and above the internal loop (Fig. 3a) and cannot be globally fitted to a single process (Supplementary Table 1). Rather, at least two distinct ESs (ES1 and ES2) need to be invoked that are sensed by residues above (ES1, $p_{ES1} \sim 9\%$, $\tau_{ES1} = 1/k_{-1} \approx 120 \mu\text{s}$) and below (ES2, $p_{ES2} \approx 2\%$, $\tau_{ES2} = 1/k_{-2} \sim 200 \mu\text{s}$) the internal loop (Fig. 3a). Interestingly, MC-Fold also predicts a complex energy landscape for SL1m with several isoenergetic secondary structures that feature variable degrees of upward or downward migration of the bulge (Supplementary Fig. 3). This, together with the ES carbon chemical shift fingerprints and MCSF analysis, led us to deduce structures for ES1 and ES2 that feature upward and downward migration of the bulge, respectively (Supplementary Discussion).

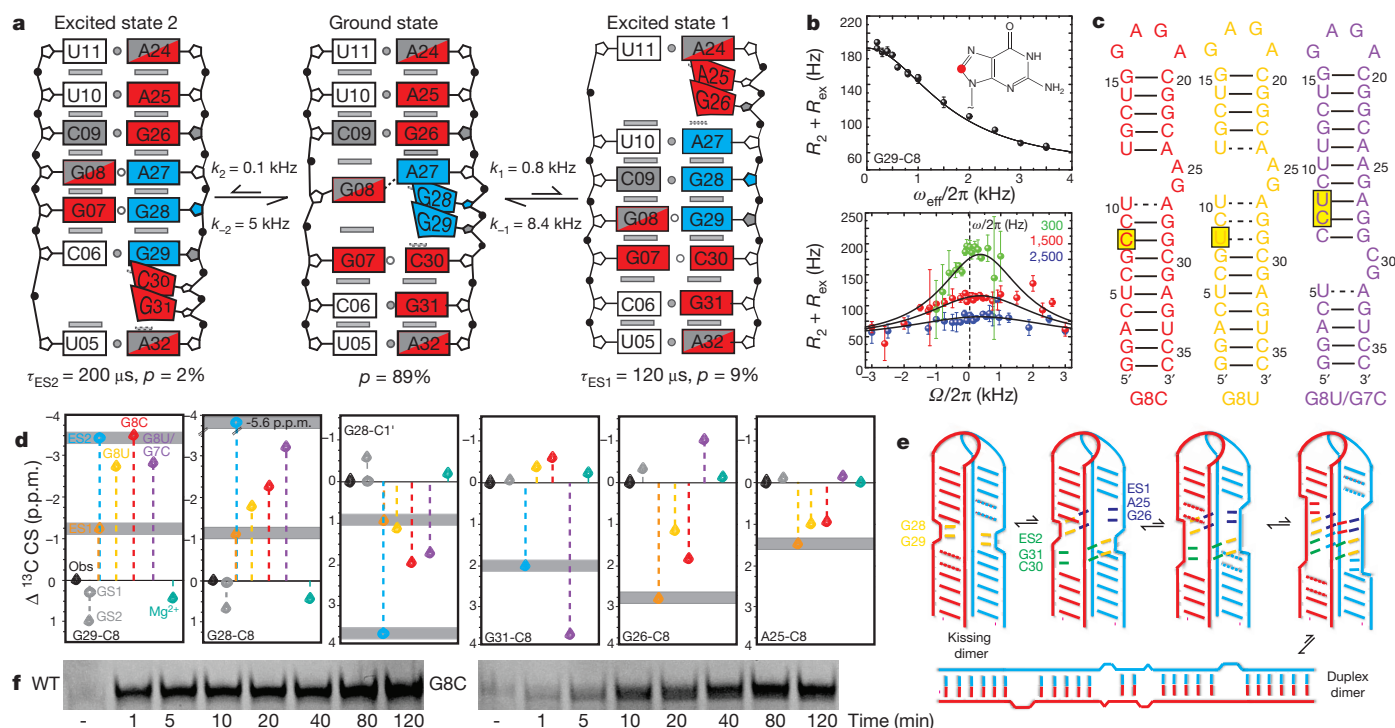


Figure 3 | Two mutually exclusive excited-state structures in HIV-1 stem-loop 1. **a**, GS and ES structures of SL1m. Chemical shift fingerprints are colour-coded as in Fig. 1a. **b**, Example relaxation dispersion profile (as in Fig. 1b). **c**, Mutant mimics of GS and ES. **d**, Comparison of carbon chemical shifts for the

In ES1, the bulge migrates upward by 3 base pairs^{43–46}. Here, G29-G28 swap base-pairing partners with A27-G26, A27 swaps with A25, and G26-A25 are bulged out (Fig. 3a). We stabilized ES1 using two point mutants (SL1m(G8C) and SL1m(G8U)) that replace the ES G8•G29 mismatch with the more stable C8•G29 and U8•G29 base pairs (Fig. 3c). Both mutants adopted the ES1 structure as verified by NMR (Supplementary Fig. 4), and relative to wild-type SL1m resulted in large changes in carbon chemical shifts for residues within (G28 and G29) and above (A25, G26 and A27) the internal loop that are directed towards the ES chemical shifts (Fig. 3d and Supplementary Fig. 5). In ES2, the bulge migrates downward by 2 base pairs. Here, G28-G29 swap base-pairing partners with C30-G31, which are now bulged out (Fig. 3a). We stabilized ES2 by replacing the ES2 G7•G28/G8•A27 mismatches with C7•G28/U8•A27 WC base pairs (Fig. 3c). This double mutant (SL1m(G7C/G8U)) adopted the proposed ES2 structure as verified by NMR (Supplementary Fig. 4) and resulted in large changes in the carbon chemical shifts for residues within (G28 and G29) and below (C30 and G31) the internal loop that are directed towards the ES chemical shifts (Fig. 3d). Mutant mimics of ES1 and ES2 induce similar chemical shift perturbations for G28 (C8 and C1') and G29 (C8), as expected given that they form base pairs in the two cases (Fig. 3d, Supplementary Fig. 5 and Supplementary Discussion). Notably, mutants that stabilize residues above the bulge in their ES conformation also stabilize residues below the bulge in their GS conformation and vice versa (Fig. 3d and Supplementary Fig. 5). This supports the mutual exclusivity of ES1 and ES2 (Fig. 3a); 'trapping' the bulge in the upper (or lower) helix prevents downward (or upward) migration and therefore traps residues in the lower (or upper) helix in their GS.

Together, the GS, ES1 and ES2 define a moving zipper in which bulge residues invade base pairs in the upper or lower helix. Remarkably, an analogous process, if carried out in an intermolecular manner between two SL1 monomers, naturally leads to isomerization

ESs, GS and mutant mimics. **e**, Proposed mechanism for spontaneous kissing-duplex isomerization. **f**, Native gel showing the reduction in isomerization rate caused by inhibiting exchanging conformations (see Supplementary Fig. 8).

and duplex formation most probably through a previously proposed quadruplex-like intermediate³⁹ (Fig. 3e). Here, bulged-out G28 and G29 can invade base pairs in the upper or lower helix in another monomer to generate ES1- or ES2-like intermolecular base pairs (Fig. 3e). The bulged-out G26 and A25 or C30 and G31 can, in turn, carry out further intermolecular strand invasions, and this process can be repeated to generate a duplex dimer (Fig. 3e). In support of this important role for ES1 and ES2 in SL1 isomerization, mutations that trap ES1 or inhibit formation of ES2 significantly diminish the rate of isomerization, whereas control sequences that preserve the stability of the stem-loop without disrupting conformational exchange show little to no effect (Fig. 3f and Supplementary Fig. 8). Thus, transitions between the GS and ES can promote ATP-independent changes in RNA secondary structure without disrupting the structural integrity of entire hairpins, which may be required for other functions, such as the formation of kissing dimers in SL1.

Compared to secondary structural transitions observed in many regulatory RNA switches^{47,48}, transitions between the ground and excited states uncovered here involve much more localized changes in RNA structure, occur at rates that are two-to-four orders of magnitude faster, and do not require assistance from external factors. Thus, they can meet unique demands in biological circuits and macromolecular machines. The ESs also present new drug targets and offer new opportunities in the engineering of RNA-based devices. Line-broadening indicative of ESs is routinely observed in NMR spectra of RNA and we therefore predict that RNA ESs exist in great abundance throughout the transcriptome. By combining NMR data with structure prediction tools, it should be possible to determine the three-dimensional structures of RNA ESs at atomic resolution.

METHODS SUMMARY

Detailed methods on RNA sample preparation and assignment, NMR relaxation dispersion data collection and analysis, and isomerization assays can be found in Methods.

Full Methods and any associated references are available in the online version of the paper.

Received 13 June; accepted 10 August 2012.

Published online 7 October 2012.

- Palmer, A. G. & Massi, F. Characterization of the dynamics of biomacromolecules using rotating-frame spin relaxation NMR spectroscopy. *Chem. Rev.* **106**, 1700–1719 (2006).
- Baldwin, A. J., Hansen, D. F., Vallurupalli, P. & Kay, L. E. Measurement of methyl axis orientations in invisible, excited states of proteins by relaxation dispersion NMR spectroscopy. *J. Am. Chem. Soc.* **131**, 11939–11948 (2009).
- Neudecker, P. *et al.* Structure of an intermediate state in protein folding and aggregation. *Science* **336**, 362–366 (2012).
- Henzler-Wildman, K. & Kern, D. Dynamic personalities of proteins. *Nature* **450**, 964–972 (2007).
- Sugase, K., Dyson, H. J. & Wright, P. E. Mechanism of coupled folding and binding of an intrinsically disordered protein. *Nature* **447**, 1021–1025 (2007).
- Korzhnev, D. M., Religa, T. L., Banachewicz, W., Fersht, A. R. & Kay, L. E. A transient and low-populated protein-folding intermediate at atomic resolution. *Science* **329**, 1312–1316 (2010).
- Li, P., Martins, I. R. S., Amarasinghe, G. K. & Rosen, M. K. Internal dynamics control activation and activity of the autoinhibited Vav DH domain. *Nature Struct. Biol.* **15**, 613–618 (2008).
- Boehr, D. D., McElheny, D., Dyson, H. J. & Wright, P. E. The dynamic energy landscape of dihydrofolate reductase catalysis. *Science* **313**, 1638–1642 (2006).
- Hansen, A. L., Nikolova, E. N., Casiano-Negroni, A. & Al-Hashimi, H. M. Extending the range of microsecond-to-millisecond chemical exchange detected in labeled and unlabeled nucleic acids by selective carbon R(1rho) NMR spectroscopy. *J. Am. Chem. Soc.* **131**, 3818–3819 (2009).
- Massi, F., Johnson, E., Wang, C., Rance, M. & Palmer, A. G. NMR $R_{1\rho}$ rotating-frame relaxation with weak radio frequency fields. *J. Am. Chem. Soc.* **126**, 2247–2256 (2004).
- Korzhnev, D. M., Orekhov, V. Y. & Kay, L. E. Off-resonance $R_{1\rho}$ NMR studies of exchange dynamics in proteins with low spin-lock fields: An application to a Fyn SH3 domain. *J. Am. Chem. Soc.* **127**, 713–721 (2005).
- Nikolova, E. N. *et al.* Transient Hoogsteen base pairs in canonical duplex DNA. *Nature* **470**, 498–502 (2011).
- Hoogstraten, C. G., Wank, J. R. & Pardi, A. Active site dynamics in the lead-dependent ribozyme. *Biochemistry* **39**, 9951–9958 (2000).
- Johnson, J. E. & Hoogstraten, C. G. Extensive backbone dynamics in the GCAA RNA tetraloop analyzed using C-13 NMR spin relaxation and specific isotope labeling. *J. Am. Chem. Soc.* **130**, 16757–16769 (2008).
- Blad, H., Reiter, N. J., Abildgaard, F., Markley, J. L. & Butcher, S. E. Dynamics and metal ion binding in the U6 RNA intramolecular stem-loop as analyzed by NMR. *J. Mol. Biol.* **353**, 540–555 (2005).
- Dethoff, E. A. *et al.* Characterizing complex dynamics in the transactivation response element apical loop and motional correlations with the bulge by NMR, molecular dynamics, and mutagenesis. *Biophys. J.* **95**, 3906–3915 (2008).
- Bannwarth, S. & Gagnon, A. HIV-1 TAR RNA: the target of molecular interactions between the virus and its host. *Curr. HIV Res.* **3**, 61–71 (2005).
- Jaeger, J. A. & Tinoco, I. Jr. An NMR study of the HIV-1 TAR element hairpin. *Biochemistry* **32**, 12522–12530 (1993).
- Kulinski, T. *et al.* The apical loop of the HIV-1 TAR RNA hairpin is stabilized by a cross-loop base pair. *J. Biol. Chem.* **278**, 38892–38901 (2003).
- Farès, C., Amata, I. & Carlomagno, T. ^{13}C -detection in RNA bases: revealing structure-chemical shift relationships. *J. Am. Chem. Soc.* **129**, 15814–15823 (2007).
- Ghose, R., Marino, J. P., Wiberg, K. B. & Prestegard, J. H. Dependence of ^{13}C chemical shifts on glycosidic torsional angles in ribonucleic acids. *J. Am. Chem. Soc.* **116**, 8827–8828 (1994).
- Nozinovic, S., Furtig, B., Jonker, H. R., Richter, C. & Schwalbe, H. High-resolution NMR structure of an RNA model system: the 14-mer cUUCG tetraloop hairpin RNA. *Nucleic Acids Res.* **38**, 683–694 (2010).
- Snoussi, K. & Leroy, J.-L. Imino proton exchange and base-pair kinetics in RNA duplexes. *Biochemistry* **40**, 8898–8904 (2001).
- Parisien, M. & Major, F. The MC-Fold and MC-Sym pipeline infers RNA structure from sequence data. *Nature* **452**, 51–55 (2008).
- Legault, P. & Pardi, A. Unusual dynamics and pKa shift at the active site of a lead-dependent ribozyme. *J. Am. Chem. Soc.* **119**, 6621–6628 (1997).
- Feng, S. & Holland, E. C. HIV-1 tat trans-activation requires the loop sequence within tar. *Nature* **334**, 165–167 (1988).
- Berkhout, B. & Jeang, K. T. trans activation of human immunodeficiency virus type 1 is sequence specific for both the single-stranded bulge and loop of the trans-acting-responsive hairpin: a quantitative analysis. *J. Virol.* **63**, 5501–5504 (1989).
- Richter, S., Cao, H. & Rana, T. M. Specific HIV-1 TAR RNA loop sequence and functional groups are required for human cyclin T1-Tat-TAR ternary complex formation. *Biochemistry* **41**, 6391–6397 (2002).
- Yoshizawa, S., Fourmy, D. & Puglisi, J. Recognition of the codon-anticodon helix by ribosomal RNA. *Science* **285**, 1722–1725 (1999).
- Schmeing, T. M. & Ramakrishnan, V. What recent ribosome structures have revealed about the mechanism of translation. *Nature* **461**, 1234–1242 (2009).
- Shandrick, S. *et al.* Monitoring molecular recognition of the ribosomal decoding site. *Angew. Chem. Int. Ed.* **43**, 3177–3182 (2004).
- Fourmy, D., Recht, M., Blanchard, S. & Puglisi, J. Structure of the A site of *Escherichia coli* 16S ribosomal RNA complexed with an aminoglycoside antibiotic. *Science* **274**, 1367–1371 (1996).
- Romanowska, J., Setny, P. & Trylska, J. Molecular dynamics study of the ribosomal A-site. *J. Phys. Chem. B* **112**, 15227–15243 (2008).
- O'Connor, M., Thomas, C. L., Zimmermann, R. A. & Dahlberg, A. E. Decoding fidelity at the ribosomal A and P sites: influence of mutations in three different regions of the decoding domain in 16S rRNA. *Nucleic Acids Res.* **25**, 1185–1193 (1997).
- Dahlquist, K. D. & Puglisi, J. D. Interaction of translation initiation factor IF1 with the *E. coli* ribosomal A site. *J. Mol. Biol.* **299**, 1–15 (2000).
- Kipper, K., Hetényi, C., Sild, S., Remme, J. & Liiv, A. Ribosomal intersubunit bridge B2a is involved in factor-dependent translation initiation and translational processivity. *J. Mol. Biol.* **385**, 405–422 (2009).
- Moore, M. D. & Hu, W.-S. HIV-1 RNA dimerization: It takes two to tango. *AIDS Rev.* **11**, 91–102 (2009).
- Clever, J. L. & Parslow, T. G. Mutant human immunodeficiency virus type 1 genomes with defects in RNA dimerization or encapsidation. *J. Virol.* **71**, 3407–3414 (1997).
- Rist, M. J. & Marino, J. P. Mechanism of nucleocapsid protein catalyzed structural isomerization of the dimerization initiation site of HIV-1. *Biochemistry* **41**, 14762–14770 (2002).
- Mujeeb, A. *et al.* Nucleocapsid protein-mediated maturation of dimer initiation complex of full-length SL1 stemloop of HIV-1: sequence effects and mechanism of RNA refolding. *Nucleic Acids Res.* **35**, 2026–2034 (2007).
- Turner, K. B., Hagan, N. A. & Fabris, D. Understanding the isomerization of the HIV-1 dimerization initiation domain by the nucleocapsid protein. *J. Mol. Biol.* **369**, 812–828 (2007).
- Takahashi, K. *et al.* Structural requirement for the two-step dimerization of human immunodeficiency virus type 1 genome. *RNA* **6**, 96–102 (2000).
- Sun, X., Zhang, Q. & Al-Hashimi, H. M. Resolving fast and slow motions in the internal loop containing stem-loop 1 of HIV-1 that are modulated by Mg^{2+} binding: role in the kissing-duplex structural transition. *Nucleic Acids Res.* **35**, 1698–1713 (2007).
- Yuan, Y., Kerwood, D. J., Paoletti, A. C., Shubsda, M. F. & Borer, P. N. Stem of SL1 RNA in HIV-1: structure and nucleocapsid protein binding for a 1 x 3 internal loop. *Biochemistry* **42**, 5259–5269 (2003).
- Lawrence, D. C., Stover, C. C., Noznitsky, J., Wu, Z. & Summers, M. F. Structure of the intact stem and bulge of HIV-1 Ψ -RNA stem-loop SL1. *J. Mol. Biol.* **326**, 529–542 (2003).
- Ulyanov, N. B. NMR structure of the full-length linear dimer of stem-loop-1 RNA in the HIV-1 dimer initiation site. *J. Biol. Chem.* **281**, 16168–16177 (2006).
- Breaker, R. R. Prospects for riboswitch discovery and analysis. *Mol. Cell* **43**, 867–879 (2011).
- Dethoff, E. A., Chugh, J., Mustoe, A. M. & Al-Hashimi, H. M. Functional complexity and regulation through RNA dynamics. *Nature* **482**, 322–330 (2012).

Supplementary Information is available in the online version of the paper.

Acknowledgements E.A.D., K.P. and J.C. contributed equally to this work. We thank members of the Al-Hashimi laboratory for input. We acknowledge the Michigan Economic Development Cooperation and the Michigan Technology Tri-Corridor for the support of the purchase of a 600 MHz spectrometer. K.P. is supported by a postdoctoral Fellowship from the Swedish Research Council (VR-K2011-78PK-21662-0-12). This work was supported by the US National Institutes of Health (R01 AI066975) and by a Rackham Graduate Student Research Grant awarded by the University of Michigan.

Author Contributions H.M.A., E.A.D., K.P. and J.C. conceived the approaches to structurally characterize RNA ES and wrote the paper. E.A.D. and K.P. performed all experiments and data analyses for HIV TAR and SL1m, respectively. J.C. with assistance from A.C.-N. performed all experiments and data analyses for the A-site.

Author Information Reprints and permissions information is available at www.nature.com/reprints. The authors declare competing financial interests: details are available in the online version of the paper. Readers are welcome to comment on the online version of the paper. Correspondence and requests for materials should be addressed to H.M.A. (hashimi@umich.edu).

METHODS

Preparation and NMR resonance assignment of labelled and unlabelled RNA.

RNA samples were prepared by *in vitro* transcription using T7 RNA polymerase (Takara Mirus Bio, Inc.), uniformly $^{13}\text{C}/^{15}\text{N}$ -labelled nucleotide triphosphates (ISOTEC, Inc., Cambridge Isotope Labs) or unlabelled (Sigma-Aldrich) nucleotide triphosphates, and synthetic DNA templates (Integrated DNA Technologies, Inc.) containing the T7 promoter and sequence of interest. All RNAs were purified by 20% (w/v) denaturing polyacrylamide gel electrophoresis, using 8 M urea and $1 \times$ TBE (89 mM Tris-borate, 89 mM boric acid, 2 mM EDTA). The RNA was electro-eluted from the gel in 20 mM Tris pH 8 buffer followed by ethanol precipitation. The RNA pellet was dissolved in water, annealed by heating to 95°C for 10 min and rapid cooling on ice and exchanged into NMR buffer (15 mM sodium phosphate, 0.1 mM EDTA, and 25 mM NaCl at pH 6.4) multiple times using an Amicon Ultra-4 Centrifugal Filter Unit (Millipore Corp.). Unlabelled RNA samples (TAR(C30U), TAR(A35-DMA), TAR(A35G), A-site(Δ U95), A-site(U95-N3M)) were purchased from Dharmacon (Thermo Fisher Scientific) and Integrated DNA Technologies and dissolved in NMR buffer (15 mM sodium phosphate, 0.1 mM EDTA, 25 mM NaCl, pH 6.4). The TAR pH studies employed the following NMR buffers: pH 7.4 (15 mM sodium phosphate, 0.1 mM EDTA and 25 mM NaCl) and pH 4.6 (15 mM acetate- d_4 , 0.1 mM EDTA, and 25 mM NaCl). Resonance assignments of wild-type RNA samples were obtained from prior studies^{16,45,49} and confirmed using standard resonance assignment experiments.

Carbon $R_{1\rho}$ relaxation dispersion. All relaxation dispersion NMR experiments were performed on a Bruker Avance 600 MHz NMR spectrometer equipped with a 5-mm triple-resonance cryogenic probe. Experiments were performed at 25°C , $25/15^\circ\text{C}$, and 15°C for TAR, A-site and SL1m, respectively, using uniformly $^{13}\text{C}/^{15}\text{N}$ -labelled RNA constructs shown in Supplementary Fig. 1. For TAR, we used a second construct lacking the bulge (EII-TAR, Supplementary Fig. 1) to measure dispersion data for U31-C6 resonance, which is otherwise overlapped. For A-site, all data were measured at 25°C with the exception of A92-C2 and A93-C8, which was measured at 15°C to push the system into slower exchange and obtain more reliable data. Rotating frame carbon $R_{1\rho}$ relaxation dispersion⁹ data were measured using a 1D acquisition scheme that extends the sensitivity to chemical exchange into millisecond timescales relative to conventional 2D relaxation dispersion methods^{9–11}. On- and off-resonance relaxation dispersion data were recorded at various offset frequencies (Ω) and spinlock powers (ω_1) (see Supplementary Table 2). The following relaxation delays were used. TAR: C30, U31, G34 and A35 C1' [0, 6 (2 \times), 14, 24 (2 \times) ms]; G32 C1' [0, 12 (2 \times), 30, 50 (2 \times) ms]; G33 C1' [0, 14 (2 \times), 34, 55 (2 \times) ms]; U31 C6 (measured on EII-TAR) [0, 7 (2 \times), 14, 28 (2 \times) ms]; G32 and A35 C8 [0, 10 (2 \times), 21, 34, 45, 55 (2 \times) ms]; G33 C8 [0, 8 (2 \times), 20, 35 (2 \times) ms]; G34 C8 [0, 5 (2 \times), 11, 20 (2 \times) ms]. A-site: G05 C8, G91 C1' [0, 8, 16, 30, 36 (2 \times) ms]; A92 C1'/C2/C8, G94C [0, 8, 16, 24, 32 (2 \times) ms]; A93 C1', U95 C6 [0, 4, 8, 14, 20 (2 \times) ms]; A93 C8 [0, 8, 22, 34, 44 (2 \times) ms]; C96 C6 [0, 8, 18, 24 ms]. SL1m: A3 C2 [0, 8 (2 \times), 10 ms], G7 C8 [0, 8 (2 \times), 16 ms], G8 C8 [0, 3.3 (2 \times), 5 ms], U9 C6 [0, 7 (2 \times), 12 ms], A24 C8 [0, 9 (2 \times), 12 ms], A24 C2 [0, 12, 16 (2 \times) ms], A25 C8 [0, 10, 14 (2 \times) ms], A25 C2 [0, 8 (2 \times), 12 ms], G26 C8 [0, 1.5, 5 (2 \times), 17 ms], G26 C1' [0, 12 (2 \times) ms], A27 C8 [0, 4, 10, 17, 25 (2 \times) ms], A27 C2 [0, 4, 10, 17, 25 (2 \times) ms], G28 C8 [0, 11, 14 (2 \times) ms], G28 C1' [0, 7 (2 \times), 9 ms], G29 C8 [0, 6, 8 (2 \times) ms], G29 C1' [0, 7 (2 \times) ms], C30 C6 [0, 5 (2 \times), 14 ms], G31 C8 [0.3, 11 (2 \times), 15 ms], A32 C8, U34C6 A32 C2, [0, 10 (2 \times), 15 ms]; G33 C8 [0, 12 (2 \times), 15 ms].

Data points that meet C-C Hartmann–Hahn matching conditions were omitted from analysis as previously described⁹. Data were processed using nmrPipe⁵⁰ and the $R_{1\rho}$ values were computed by fitting the resonance intensities with mono-exponential decays using Mathematica 6.0 script⁵¹ (Wolfram Research, Inc.). The relaxation dispersion data were fitted¹ to fast exchange (equation (1), three independent variables), asymmetric exchange (equation (2), five independent variables), and the Laguerre equation (equation (3), five independent variables) using Origin 8.5.1 (OriginLab).

Fast exchange ($k_{\text{ex}} \gg \Delta\omega$):

$$R_{1\rho} = R_1 \cos^2 \theta + R_2 \sin^2 \theta + \frac{\sin^2 \theta \Phi k_{\text{ex}}}{\omega_{\text{eff}}^2 + k_{\text{ex}}^2}$$

where

$$\begin{aligned} \Phi &= p_{\text{GS}} p_{\text{ES}} \Delta\omega^2 \\ \Delta\omega &= \Omega_{\text{ES}} - \Omega_{\text{GS}} \\ k_{\text{ex}} &= k_1 + k_{-1} \end{aligned} \quad (1)$$

Asymmetric exchange ($p_{\text{GS}} \gg p_{\text{ES}}$):

$$R_{1\rho} = R_1 \cos^2 \theta + R_2 \sin^2 \theta + \frac{\sin^2 \theta p_{\text{GS}} p_{\text{ES}} \Delta\omega^2 k_{\text{ex}}}{\omega_{\text{GS}}^2 \omega_{\text{ES}}^2 / \omega_{\text{eff}}^2 + k_{\text{ex}}^2} \quad (2)$$

Laguerre equation (general):

$$R_{1\rho} = R_1 \cos^2 \theta + R_2 \sin^2 \theta + \frac{\sin^2 \theta p_{\text{GS}} p_{\text{ES}} \Delta\omega^2 k_{\text{ex}}}{\omega_{\text{GS}}^2 \omega_{\text{ES}}^2 / \omega_{\text{eff}}^2 + k_{\text{ex}}^2 - \sin^2 \theta p_{\text{GS}} p_{\text{ES}} \Delta\omega^2 \left(1 + \frac{2k_{\text{ex}}^2 (p_{\text{GS}} \omega_{\text{GS}}^2 + p_{\text{ES}} \omega_{\text{ES}}^2)}{\omega_{\text{GS}}^2 \omega_{\text{ES}}^2 + \omega_{\text{eff}}^2 k_{\text{ex}}^2} \right)} \quad (3)$$

where,

$$\omega_{\text{eff}}^2 = \Omega^2 + \omega_1^2, \omega_{\text{GS}}^2 = (\Omega_{\text{GS}} - \omega_{\text{rf}})^2 + \omega_1^2, \omega_{\text{ES}}^2 = (\Omega_{\text{ES}} - \omega_{\text{rf}})^2 + \omega_1^2$$

R_1 and R_2 are the intrinsic longitudinal and transverse relaxation rates, respectively (assumed to be identical for GS and ES); $\Omega = \Omega_{\text{obs}} - \omega_{\text{rf}}$ is the offset of the spin-lock carrier frequency (ω_{rf}) from the averaged resonance frequency (Ω_{obs}); ω_{eff} is the effective spin-lock strength; $\theta = \arctan(\omega_1/\Omega)$; $\Omega_{\text{obs}} = p_{\text{GS}}\Omega_{\text{GS}} + p_{\text{ES}}\Omega_{\text{ES}}$, where p_{GS} (p_{ES}) is the ground (excited) state fractional population ($p_{\text{GS}} + p_{\text{ES}} = 1$); $k_{\text{ex}} = k_1 + k_{-1}$ is the exchange rate constant for a two-state equilibrium, where $k_1 = p_{\text{ES}}k_{\text{ex}}$ and $k_{-1} = p_{\text{GS}}k_{\text{ex}}$ are the forward and reverse rate constants, respectively. Note that whereas for $p_{\text{ES}} < 2\%$, $\Omega_{\text{obs}} \approx \Omega_{\text{GS}}$, this is not the case for significantly populated ESs, such as TAR and SL1m-ES1 ($\sim 13\%$ and 9% , respectively).

Model selection was carried out using an *F*-test (Supplementary Table 1), which uses chi-squared (χ^2), applying the Levenberg–Marquardt minimization algorithm, to determine the feasibility of a model (for example, individual fits) versus a more complex model (that is, shared-parameter/3-state fits, number of independent variables equal number of reported parameters) expanded from the first model. In general, similar $\Delta\omega$ values were obtained when fitting dispersion data using asymmetric (equation (2)) and Laguerre (equation (3)) equations. Errors were determined using standard Monte Carlo simulations⁵² and verified using Bootstrapping approaches for error analysis^{52,53} (data not shown). For TAR, all fast exchanging resonances were combined in a global fit except U31-C6. For the A-site, four resonances (G91-C1', A92-C1', U95-C6, C96-C6) can be globally fitted according to the *F*-test and the remaining resonances (G05-C8, A92-C8, G94-C8) can be included into the global fit without affecting the resulting fitted parameters (values are within error when globally fitting four or seven resonances). A-site data measured at 15°C were fitted individually although similar $\Delta\omega$ values were obtained when these data were included in global fits with other data measured at 25°C . The $\Delta\omega$ values obtained from both individual and global fits are shown for A92-C2 in Supplementary Fig. 5. For SL1, the G26-C8, A25-C8 and A25-C2 were combined in a global fit to characterize ES1, and G31-C8, C30-C6 and G7-C8 were combined in a global fit to characterize ES2. G28-C8, G28-C1' and G29-C8 were included in a global fit to ES1 and ES2 using a three-state model. A27-C8 and G8-C8 were fitted individually using single and three-state exchange models. $\Delta\omega$ values obtained for dispersion profiles with $R_{\text{ex}} < 5$ Hz or that yielded ambiguous signs for $\Delta\omega$ during the Monte Carlo error analysis were deemed unreliable (these include A-site: G05-C1', U06-C1', U06-C6, C07-C1' and A08-C2; SL1m: G29-C1' and G26-C1'). The sign of $\Delta\omega$ for TAR U31-C6 was deduced from the pH-dependent perturbations. Data that failed the above criteria but that could be included in global fitting as judged using an *F*-test were included in the global fitting (TAR: C30-C1') or individually fitted assuming k_{ex} and p_{ES} values determined by globally fitting the dispersion data (SL1m, C30-C6 and G7-C8, and TAR, U31-C6).

Thermodynamic analysis. The free energy difference between the GS and ES (ΔG^{ES}) and between the GS and transition state (ΔG^{TS}) was computed using (with $\Delta G^{\text{GS}} = 0$):

$$\begin{aligned} \Delta G^{\text{ES}} &= \left(-\ln \left(\frac{k_1 h}{k_B T} \right) RT \right) - \left(-\ln \left(\frac{k_{-1} h}{k_B T} \right) RT \right) \\ \Delta G^{\text{TS}} &= -\ln \left(\frac{k_1 h}{k_B T} \right) RT \end{aligned}$$

where $k_{1/-1}$ are rate constants, h is Planck's constant, k_B is Boltzmann's constant, R is the gas constant and T is temperature.

SL1 isomerization assay. SL1 isomerization assays were performed closely following the procedure described previously⁴⁰. Briefly, SL1 RNA samples (SL1, SL1(G8C), SL1(tGC), SL1(eGC)) (Fig. 1e and Supplementary Fig. 8) containing the wild-type apical loop were purchased from Integrated DNA Technologies, Inc. RNA samples were dissolved in water to a concentration of $5 \mu\text{M}$, heated to 95°C for 3 min and placed on ice for 30 min. Subsequently, 50% (v/v) $2 \times$ dimerization buffer (20 mM sodium phosphate, pH 6.4, 100 mM NaCl, and 0.2 mM MgCl_2) was added to produce a final RNA concentration of $2.5 \mu\text{M}$, and the sample incubated at 55°C or on ice for a variable amount of time. Native gels

were run using TBE buffer and control with TBM (TBE with no EDTA but 10 mM MgCl_2) as previously described⁴⁰ and detected with ethidium bromide staining. **MC-fold predictions of RNA secondary structure.** All RNA secondary structures were predicted based on sequence using the program MC-Fold²⁴ (<http://www.major.irc.ca/MC-Fold/>) with standard input options.

49. Fourmy, D., Yoshizawa, S. & Puglisi, J. D. Paromomycin binding induces a local conformational change in the A-site of 16 S rRNA. *J. Mol. Biol.* **277**, 333–345 (1998).
50. Delaglio, F. *et al.* Nmrpipe—a multidimensional spectral processing system based on Unix Pipes. *J. Biomol. NMR* **6**, 277–293 (1995).
51. Spyropoulos, L. A suite of Mathematica notebooks for the analysis of protein main chain 15N NMR relaxation data. *J. Biomol. NMR* **36**, 215–224 (2006).
52. Meinholt, D. W. & Wright, P. E. Measurement of protein unfolding/refolding kinetics and structural characterization of hidden intermediates by NMR relaxation dispersion. *Proc. Natl Acad. Sci. USA* **108**, 9078–9083 (2011).
53. Vallurupalli, P., Bouvignies, G. & Kay, L. E. Increasing the exchange time-scale that can be probed by CPMG relaxation dispersion NMR. *J. Phys. Chem. B* **115**, 14891–14900 (2011).